



# Adaptive phase field simulation of quasi-static crack propagation in rocks

Shuwei Zhou<sup>a,b,\*</sup>, Xiaoying Zhuang<sup>b,c</sup>

<sup>a</sup> Institute of Structural Mechanics, Bauhaus-University Weimar, Weimar 99423, Germany

<sup>b</sup> Department of Geotechnical Engineering, College of Civil Engineering, Tongji University, Shanghai 200092, PR China

<sup>c</sup> Institute of Continuum Mechanics, Leibniz University Hannover, Hannover 30167, Germany

Received 4 February 2018; received in revised form 16 April 2018; accepted 29 April 2018

Available online 18 June 2018

## Abstract

In this study, we present an adaptive phase field method (APFM) for modeling quasi-static crack propagation in rocks. Crack initiation due to positive strains is considered, and a numerical simulation is implemented using a commercial software, COMSOL Multiphysics. Two benchmark tests are first examined, namely, a single-edge-notched square plate subjected to respective tension and shear loadings. The crack propagation in Brazil splitting tests, 2D notched semi-circular bend (NSCB) tests, and 3D NSCB tests are subsequently simulated and analyzed. All the numerical examples indicate that the propagation of the cracks is autonomous and external fracture criteria are not required for phase field modeling. Furthermore, the adaptive remeshing scheme reduces unnecessary global mesh refinement and exhibits good adaptability for fracture modeling. The simulations are in good agreement with the experimental observations, and thereby indicate the feasibility and practicability of the APFM in rocks (even in 3D cases).

© 2018 Tongji University and Tongji University Press. Production and hosting by Elsevier B.V. on behalf of Owner. This is an open access article under the CC BY-NC-ND license (<http://creativecommons.org/licenses/by-nc-nd/4.0/>).

**Keywords:** Phase field; Adaptive scheme; Rock; Crack propagation

## 1 Introduction

Fracture mechanics is extensively applied in rock engineering because fracture-induced failure is an important threat to engineering safety (Anderson, 2005). However, the prediction of fracture propagation in rocks is challenging because rock masses correspond to a material that has several pre-existing flaws such as micro cracks, voids and soft minerals. A few studies that examined crack propagation in rocks include Bobet and Einstein (1998); Wong et al. (2001); Sagong and Bobet (2002); Wong and Einstein (2009); Park and Bobet (2009, 2010); Lee and

Jeon (2011); and Zhou et al. (2014). All the aforementioned studies focus on laboratory tests with only simple loads because it is difficult to implement increasingly complicated load cases in practical tests. Therefore, numerical methods are a good alternative to examine fracture problems in rocks. It is essential to introduce a few cutting-edge numerical technologies in rock mechanics because they are less expensive than experimental tests and can provide new physical insights that are difficult to gain through ‘pure’ experimental testing.

Numerical methods for fracture can be classified into discrete and continuous approaches. Classical representatives of the first approach include efficient remeshing techniques (Areias & Rabczuk, 2017; Areias et al., 2013; Areias & Rabczuk, 2013), strain-softening elements (Areias et al., 2014), extended finite element method (Nanthakumar et al., 2014; Møes & Belytschko, 2002), phantom node

\* Corresponding author at: Department of Geotechnical Engineering, College of Civil Engineering, Tongji University, Shanghai 200092, PR China.

E-mail address: zhoushuwei1016@126.com (S. Zhou).

method (Rabczuk, Zi, Gertenberger, et al., 2008; Chau-Dinh et al., 2012; Vu-Bac et al., 2013), and specific mesh-free methods (Rabczuk, Areias, et al., 2007; Rabczuk & Zi, 2007; Rabczuk, Bordas, et al., 2007; Rabczuk, Zi, Gertenberger, et al., 2008; Rabczuk & Samaniego, 2008; Rabczuk, Zi, Bordas, et al., 2008; Amiri et al., 2014). Discrete crack approaches include the cracking particles method (CPM) (Rabczuk & Belytschko, 2004, 2007; Rabczuk et al., 2010), peridynamics (Rabczuk & Ren, 2017), and dual-horizon peridynamics (Ren et al., 2016, 2017). The aforementioned approaches share the simplicity of continuous approaches, and they do not require any explicit representation of the crack surface or any crack tracking algorithm. In an element-erosion method (Belytschko & Lin, 1987; Johnson & Stryk, 1987), the stress in a fractured element is directly set as zero. This treatment essentially leads to a disadvantage wherein it is not possible for the element-erosion method to accurately simulate crack branching (Song et al., 2008). Gradient models (Thai et al., 2016), nonlocal models (Pijaudier-Cabot et al., 2004), models based on the screened-Poisson equation (Areias, Msekh, et al., 2016) and phase field models are typical continuous approaches to fracture (Hamdia et al., 2015; Vu-Bac et al., 2016; Areias, Rabczuk, et al., 2016; Hamdia et al., 2017; Badawy et al., 2017; Msekh et al., 2017).

In this study, we focus on the phase field model (PFM) (Bourdin et al., 2008; Miehe, Hofacker, et al., 2010; Miehe, Welschinger, et al., 2010; Hesch & Weinberg, 2014; Borden et al., 2012) to model quasi-static crack propagation in rocks. An original study exploring the PFM was presented by Bourdin et al. (2008) although the PFM was fully developed by Miehe, Hofacker, et al. (2010) in a thermodynamic consistent framework. Continuous attention focuses on PFMs due to their relatively easy implementation and extension to multi-physics problems. The PFM does not model the crack as a sharp discontinuity and instead uses a scalar field (so-called phase field) to smear the crack over the calculation domain. Hence, the crack region is similar to a 'damage-like' zone. The crack width is controlled by a length-scale parameter and propagation of the crack is automatically determined by solving a differential equation (Borden et al., 2012). As a continuous approach, the PFM does not require any external fracture criteria or algorithm to track the fracture surface. This advantage of the PFM attracts increasing attention in modeling the branching and merging of multiple cracks when compared with other numerical approaches.

Conventional phase field methods need an extremely fine mesh to obtain accurate results. For example, globally refined meshes involve extensive computational costs. However, the mesh local-refinement technique requires the crack path a priori, and this is often unknown. Therefore, an adaptive mesh refinement method coupled with the phase field method (the adaptive phase field method) is applied in the present study to simulate quasi-static crack propagation. We implement the adaptive phase field

method (APFM) in commercial software, COMSOL Multiphysics, and test the performance of the APFM in the following two benchmark tests: a single-edge-notched square plate subjected to tension and shear loadings. We subsequently apply the adaptive phase field model and simulate the quasi-static cracks in three cases of rocks, namely, Brazilian splitting tests, 2D notched semi-circular bend (NSCB) tests, and 3D NSCB tests. All the examples tested exhibit good applicability of the APFM in modeling quasi-static cracks in rocks.

This paper is outlined as follows. The adaptive phase field model for quasi-static brittle fractures is presented in Section 2. The numerical implementation coupled with COMSOL is presented in Section 3. Subsequently, we test the adaptive phase field modeling through two classical benchmark tests in Section 4. Simulations of propagation of quasi-static cracks in three rock cases are shown in Section 5, and Section 6 presents the study conclusions.

## 2 Adaptive phase field modeling

### 2.1 Phase field theory of brittle fracture

Griffith's theory for brittle fracture (Anderson, 2005) states that the crack propagation occurs when the stored energy in a body  $\Omega \subset \mathbb{R}^d$  ( $d \in \{1, 2, 3\}$ ) exceeds the fracture resistance of the body. Therefore, for quasi-static problems, the crack propagation is considered as a process to minimize free energy  $L$ :

$$L = \int_{\Omega} \psi_e(\boldsymbol{\varepsilon}) d\Omega + \int_{\Gamma} G_c dS - \int_{\Omega} \mathbf{b} \cdot \mathbf{u} d\Omega - \int_{\partial\Omega_{hi}} \mathbf{f} \cdot \mathbf{u} dS, \quad (1)$$

where  $\psi_e(\boldsymbol{\varepsilon})$  denotes the elastic energy,  $\mathbf{u}$  denotes the displacement at a position  $\mathbf{x}$ ,  $\boldsymbol{\varepsilon}$  denotes the linear strain tensor,  $G_c$  denotes the critical energy release rate, and  $\mathbf{b}$  and  $\mathbf{f}$  denote the body and surface forces acting on the body  $\psi_e(\boldsymbol{\varepsilon})$ , respectively.

$$\phi = \begin{cases} 0, & \text{if material is intact} \\ 1, & \text{if material is cracked.} \end{cases} \quad (2)$$

The phase field method (Miehe, Hofacker, et al., 2010) indicates that the crack surface density per unit volume of the solid is given as follows:

$$\gamma(\phi, \nabla\phi) = \frac{\phi^2}{2l_0} + \frac{l_0}{2} |\nabla\phi|^2, \quad (3)$$

where  $l_0$  denotes the length scale parameter that controls the transition region of the phase field, and thereby reflects the width of the crack. Thus, the crack region exhibits a larger width when  $l_0$  increases. The fracture energy in the energy functional is thereby approximated as follows:

$$\int_{\Gamma} G_c dS = \int_{\Omega} G_c \left( \frac{\phi^2}{2l_0} + \frac{l_0}{2} |\nabla\phi|^2 \right) d\Omega. \quad (4)$$

In order to capture cracks only under tension, a complete phase field method (Miehe, Welschinger, et al., 2010) requires an elastic energy based on strain decomposition as follows:

$$\boldsymbol{\varepsilon}_{\pm} = \sum_{a=1}^d \langle \varepsilon_a \rangle_{\pm} \mathbf{n}_a \otimes \mathbf{n}_a, \quad (5)$$

where  $\boldsymbol{\varepsilon}_+$  and  $\boldsymbol{\varepsilon}_-$  denote the respective tensile and compressive strain tensors,  $\varepsilon_a$  denotes the principal strain, and  $\mathbf{n}_a$  denotes the direction of the principal strain. The operators  $\langle \cdot \rangle_{\pm}$  are defined as follows:  $\langle \cdot \rangle_{\pm} = (\cdot \pm |\cdot|)/2$ . Based on the strain decomposition, the positive and negative elastic energy densities are expressed as follows:

$$\psi_{\varepsilon}^{\pm}(\boldsymbol{\varepsilon}) = \frac{\lambda}{2} \langle \text{tr}(\boldsymbol{\varepsilon}) \rangle_{\pm}^2 + \mu \text{tr}(\boldsymbol{\varepsilon}_{\pm}^2), \quad (6)$$

where  $\lambda > 0$  and  $\mu > 0$  denote the Lamé constants.

We refer to Borden et al. (2012) and assume the phase field to affect the elastic energy density as follows:

$$\psi_{\varepsilon}(\boldsymbol{\varepsilon}) = [(1-k)(1-\phi)^2 + k] \psi_{\varepsilon}^+(\boldsymbol{\varepsilon}) + \psi_{\varepsilon}^-(\boldsymbol{\varepsilon}), \quad (7)$$

where  $0 < k \ll 1$  denotes a stability parameter that prevents numerical singularities.

## 2.2 Governing equations

The energy functional  $L$  is re-expressed as follows:

$$L = \int_{\Omega} \left\{ [(1-k)(1-\phi)^2 + k] \psi_{\varepsilon}^+(\boldsymbol{\varepsilon}) + \psi_{\varepsilon}^-(\boldsymbol{\varepsilon}) \right\} d\Omega + \int_{\Omega} G_c \left( \frac{\phi^2}{2l_0} + \frac{l_0}{2} |\nabla \phi|^2 \right) d\Omega - \int_{\Omega} \mathbf{b} \cdot \mathbf{u} d\Omega - \int_{\partial\Omega_{hi}} \mathbf{f} \cdot \mathbf{u} dS. \quad (8)$$

By applying the first variation of the functional  $\delta L = 0$ , the strong form of the governing equations is given as follows (Borden et al., 2012):

$$\begin{cases} \text{Div}(\boldsymbol{\sigma}) + \mathbf{b} = 0 \\ \left[ \frac{2l_0(1-k)\psi_{\varepsilon}^+}{G_c} + 1 \right] \phi - l_0^2 \nabla^2 \phi = \frac{2l_0(1-k)\psi_{\varepsilon}^+}{G_c}, \end{cases} \quad (9)$$

where  $\boldsymbol{\sigma}$  denotes Cauchy stress tensor  $\boldsymbol{\sigma} = \partial_{\varepsilon} \psi_{\varepsilon}$ .

The irreversibility condition must be satisfied in the phase field method, and a strain-history field  $H(\mathbf{x}, t)$  (Miehe, Hofacker, et al., 2010; Welschinger, et al., 2010) is introduced to ensure a monotonically increasing phase field as follows:

$$H(\mathbf{x}, t) = \max_{s \in [0, t]} \psi_{\varepsilon}^+(\boldsymbol{\varepsilon}(\mathbf{x}, s)). \quad (10)$$

By replacing  $\psi_{\varepsilon}^+$  by  $H(\mathbf{x}, t)$  in Eq. (9), the strong form is subsequently re-expressed as follows:

$$\begin{cases} \text{Div}(\boldsymbol{\sigma}) + \mathbf{b} = 0 \\ \left[ \frac{2l_0(1-k)H}{G_c} + 1 \right] \phi - l_0^2 \nabla^2 \phi = \frac{2l_0(1-k)H}{G_c}. \end{cases} \quad (11)$$

The Dirichlet and Neumann boundary conditions to solve the governing equations are presented as follows:

$$\begin{cases} \mathbf{u} = \mathbf{g} & \text{on } \partial\Omega_{gi} \\ \boldsymbol{\sigma} \cdot \mathbf{m} = \mathbf{f} & \text{on } \partial\Omega_{hi} \\ \nabla \phi \cdot \mathbf{m} = 0 & \text{on } \partial\Omega \end{cases} \quad (12)$$

$\partial\Omega_{gi}$  and  $\partial\Omega_{hi}$  denote the respective Dirichlet and Neumann boundaries of the displacement field,  $\mathbf{g}$  denotes the prescribed displacement, and  $\mathbf{m}$  denotes the outward-pointing normal vector to the boundaries.

## 2.3 Adaptive phase field method

The conventional phase field method requires an extremely fine mesh to obtain an accurate solution. For example, Miehe, Hofacker, et al. (2010) recommends a mesh size  $h < l_0$ . An excessively low  $l_0$  produces an excessive number of meshes. Therefore, globally very fine or globally refined meshes are observed in most phase field simulations. A high number of meshes can sharply increase computational costs. A good alternative is the pre-refinement mesh technique. However, this mesh local-refinement technique requires a crack path as a priori, and in factual engineering most of the crack paths are unknown to researchers. An adaptive mesh refinement method can be applied with the phase field method, and this constitutes the d adaptive phase field method. The adaptive mesh refinement does not require a priori information for the crack paths. In order to ensure crack propagation into the finer meshes, a predictor-corrector scheme for mesh adaptively should be used (Comsol, 2005). At the first step, the system is solved to predict the crack path (Badnava et al., 2018). Subsequently, a pre-specified refinement threshold is used to determine if the mesh is refined. Thus, in each element, the refinement flag is activated when the phase field reaches a predefined threshold (Badnava et al., 2018). Finally, all the fields are solved again based on the refined mesh. In each time step, the predictor-corrector mesh refinement is continuously applied unless the threshold condition is not satisfied. It should be noted that both the thresholds for the phase field are 0.85 for the 2D and 3D simulations.

## 3 COMSOL implementation

We implemented the adaptive phase field method in COMSOL Multiphysics, software for multi-field modeling. In the study, three main modules, namely, solid mechanics, history-strain, and phase field modules, are constructed. Additionally, a pre-set storage module is employed to evaluate and store intermediate field variables in a time step. The solid mechanics module is established on a linear elastic material library and used for the displacement  $\mathbf{u}$ . The stiffness matrix  $\mathbf{D}_e$  in the solid mechanics module is obtained by using the fourth order tensor  $\mathbf{D} = \partial \boldsymbol{\sigma} / \partial \boldsymbol{\varepsilon}$ . The phase field module for the phase field  $\phi$  employs a pre-defined Helmholtz equation governed module. With respect to the history strain field  $H$ , the distributed “ODEs

and DAEs” interfaces are used to construct the history-strain module. The history strain field is not solved directly. Conversely, we use a “previous solution“ solver to record the results in the previous time steps and obtain the field  $H$ .

We use a staggered (segregated) scheme to implement the adaptive phase field method, and the detailed procedure is shown in Fig. 1. The equations of displacement, history strain, and phase-field are solved independently. With respect to time integration, an implicit generalized- $\alpha$  (Comsol, 2005) method is applied. In order to accelerate the iteration convergence, the Anderson acceleration (Comsol, 2005) is employed, and the dimension of the iteration space field is set to exceed 50. The flow chart of the implementation of the adaptive phase field method is shown in Fig. 2.

#### 4 Benchmark tests

We test the adaptive phase field modeling of fractures in two 2D benchmark tests in this section.

##### 4.1 Notched square plate subjected to tension

The first benchmark test is a square plate with an initial notch that is subject to static tension loading. The benchmark test is calculated and analyzed by several researchers (Miehe, Hofacker, et al., 2010; Welschinger, et al., 2010; Hesch & Weinberg, 2014). The geometry and boundary condition are shown in Fig. 3. We apply a vertical displacement  $u$  on the upper boundary of the plate while  $u_x = 0$  is also applied. The boundary conditions are the same as those of Hesch and Weinberg (2014). The following material parameters are adopted:  $E = 210$  GPa,  $v = 0.3$ , and  $G_c = 2700$  J/m<sup>2</sup>. We select  $k = 1 \times 10^{-9}$  to avoid numerical singularity. The length parameters are  $l_0 = 7.5 \times 10^{-3}$  mm and  $1.5 \times 10^{-2}$  mm.

In order to reduce the time involved, we use a displacement increment of  $\Delta u = 1 \times 10^{-5}$  mm for the first 450 time steps while  $\Delta u = 1 \times 10^{-6}$  mm is selected for the remaining time steps. With respect to the two fixed length scale

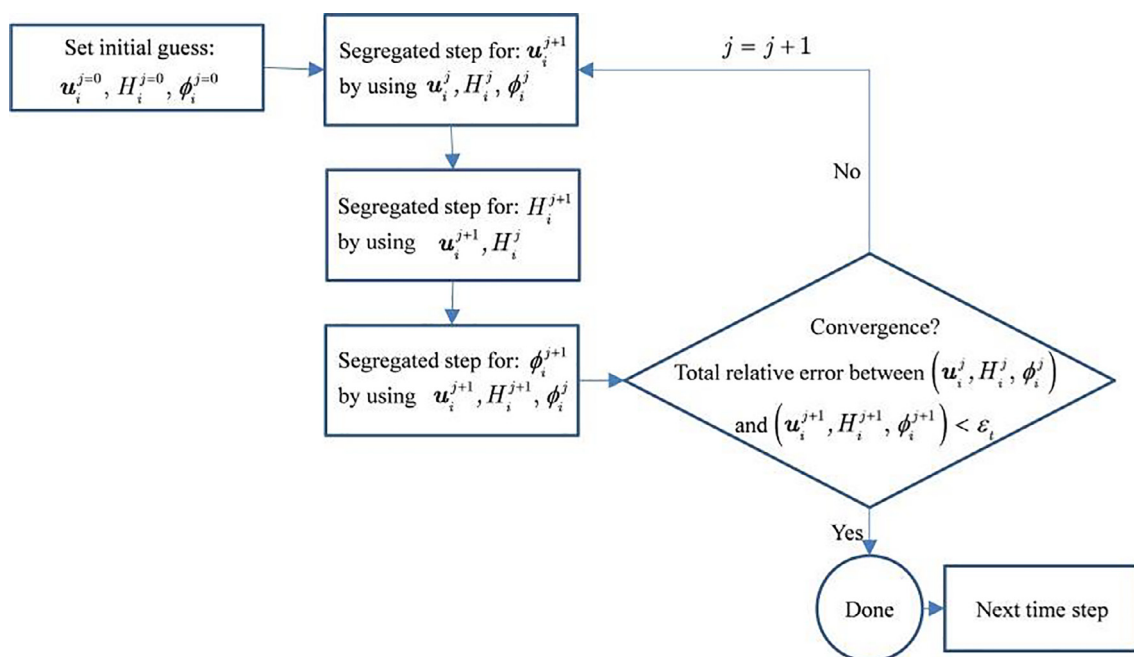


Fig. 1. Segregated scheme of the adaptive phase field method.

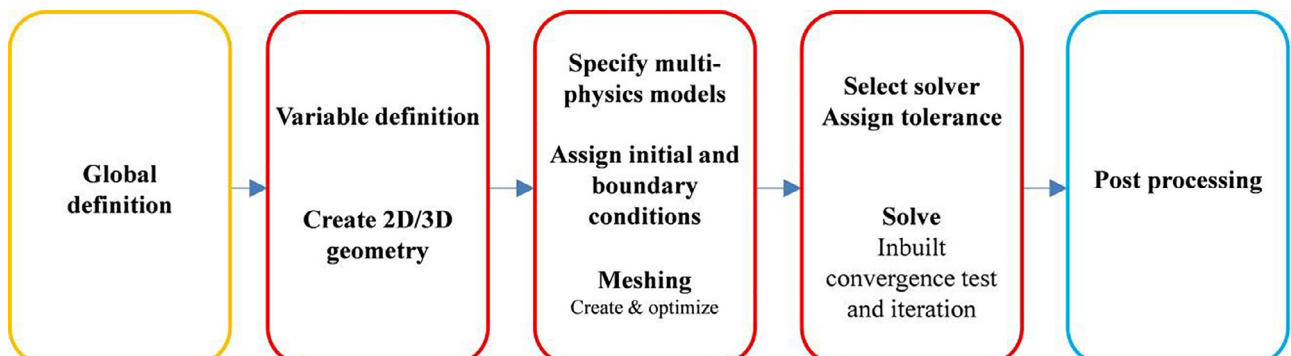


Fig. 2. COMSOL implementation of the phase field modeling.

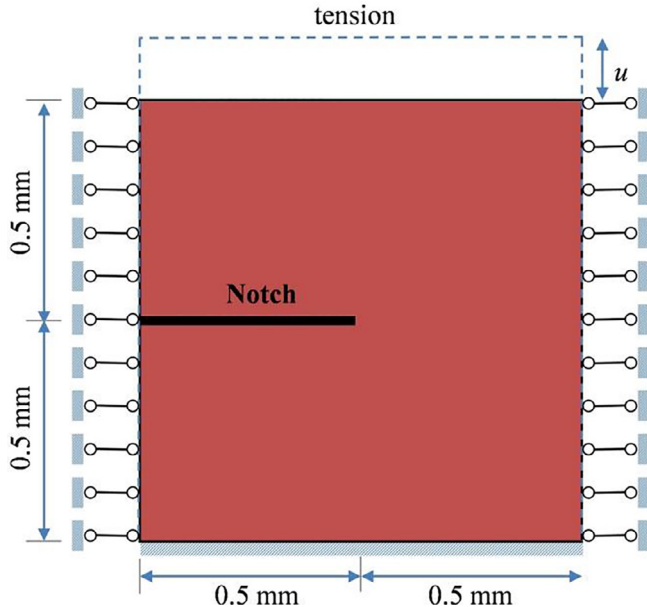


Fig. 3. Geometry and boundary condition of the single-edge-notched square plate subjected to tension.

parameters  $l_0$ , the crack patterns at different displacements are shown in Fig. 4. As expected, the cracks propagate along the horizontal direction, and a decrease in the length scale parameter leads to a less diffused crack.

Figure 5 shows the original and final meshes after the adaptive phase field method is applied. As shown in the figure, the mesh density increases around the crack paths. An obvious mesh refinement is not observed in the left part of the plate. In order to compare the adaptive phase field method, we also test the plate subjected to tension by using conventional phase field method with different meshes and displacement increments. For example, the mesh size  $h$  is changed to  $7.92 \times 10^{-3}$  and  $1.98 \times 10^{-3}$  mm, and the displacement increment is changed to  $\Delta u$  to  $2 \times 10^{-6}$  and  $5 \times 10^{-7}$  mm in the remaining time steps. The results show that mesh size and displacement increment do not affect the crack pattern. The load–displacement curves for the top edge of the plate are shown in Fig. 6. A comparison of the adaptive phase field method (APFM) and conventional phase field method (PFM) is shown in Fig. 6. As shown in the figure, increase in the mesh size and displacement increment increase the peak load. Additionally, a significantly steeper post-peak stage is observed for a smaller displacement increment.

#### 4.2 Notched square plate subjected to shear loading

The second benchmark test is the 2D notched square plate subjected to shear loading. We present the geometry and boundary conditions of the plate subjected to shear in Fig. 7. In order to reduce the time cost, we consider

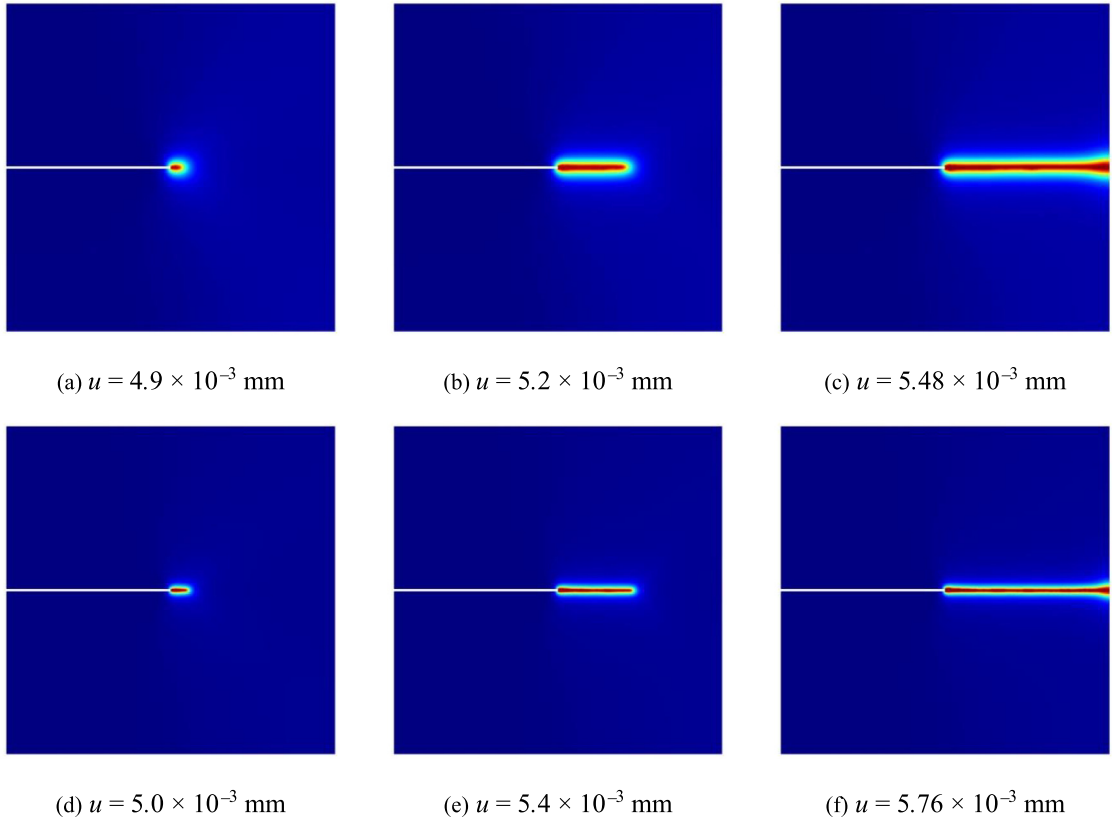


Fig. 4. Crack pattern of 2D single-edge-notched square subjected to tension: (a), (b), (c) for a length scale  $l_0$  of  $1.5 \times 10^{-2}$  mm and (d), (e), and (f) for a length scale  $l_0$  of  $7.5 \times 10^{-3}$  mm.

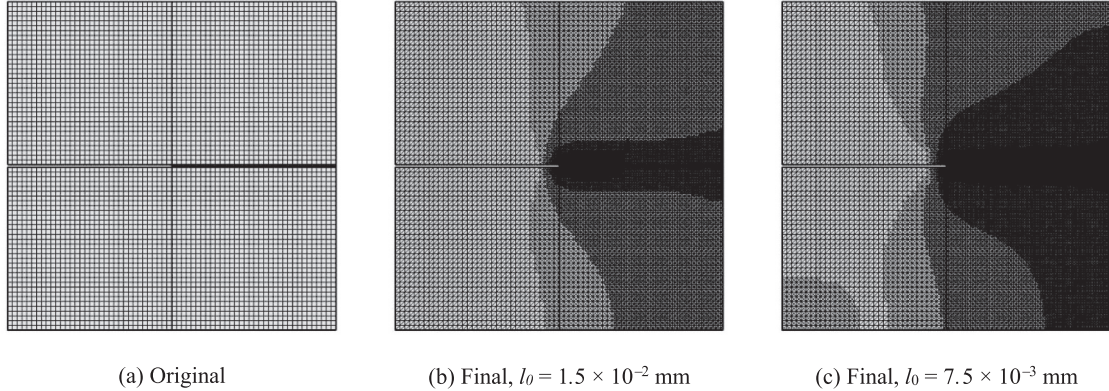


Fig. 5. Meshes of the 2D Single-edge-notched square subjected to tension.

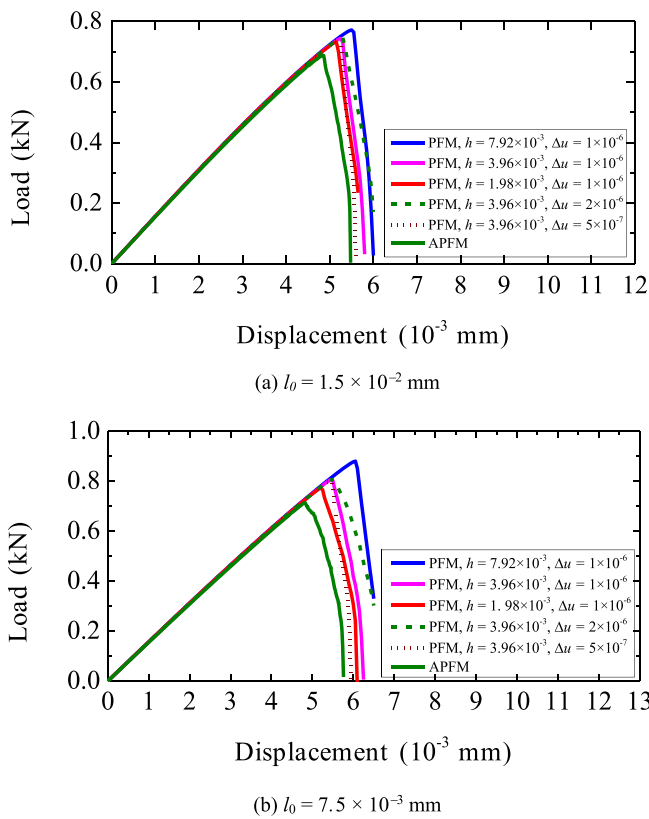


Fig. 6. Load-displacement curves of the 2D single-edge-notched square subjected to tension.

the displacement increment  $\Delta u = 1 \times 10^{-4}$  mm for the first 80 time steps and  $\Delta u = 1 \times 10^{-5}$  mm for the remaining steps. Additionally, two length scale parameters are tested as follows:  $l_0 = 1.5 \times 10^{-2}$  mm and  $l_0 = 7.5 \times 10^{-3}$  mm.

Figure 8 shows the original and final meshes when the adaptive phase field method is applied. As shown in the figure, the mesh density increases around the crack paths. The crack patterns under shear loading for the two length scale parameters are shown in Fig. 9. As expected, the crack propagates under the shear loading and the crack exhibits wider crack width when  $l_0 = 1.5 \times 10^{-2}$  mm.

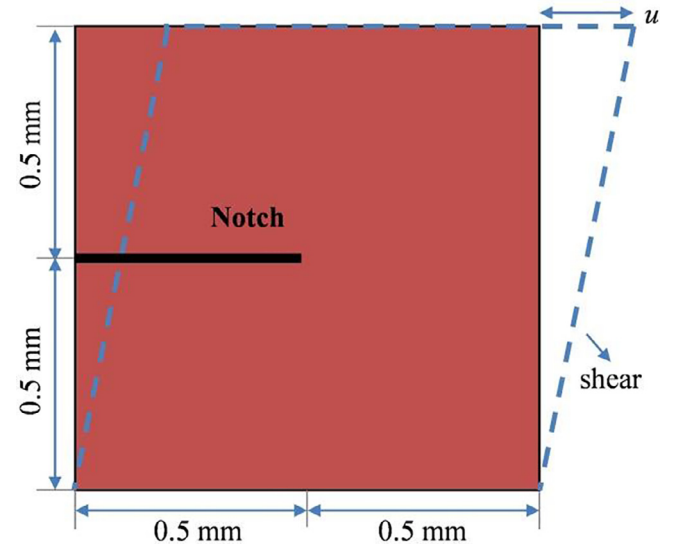


Fig. 7. Geometry and boundary condition of the single-edge-notched plate subjected to shear loading.

We also calculate the benchmark test by using different meshes and displacement increments. The load–displacement curves for the top edge of the plate are depicted in Fig. 10. We also compare the adaptive phase field method and conventional phase field method in Fig. 10. The results of Hesch and Weinberg (2014) are shown in Fig. 10 for better comparison and indicate that increases in the mesh size and displacement increment increase the peak load. Additionally, the results of the APFM are in good agreement with those of Hesch and Weinberg (2014), thereby validating the presented APFM.

## 5 Simulations of fracture propagation in rocks

### 5.1 Brazil splitting tests

Researchers commonly use a Brazil splitting test to determine the tensile strength of a rock in laboratory tests, and fracture in a Brazil specimen is extensively examined

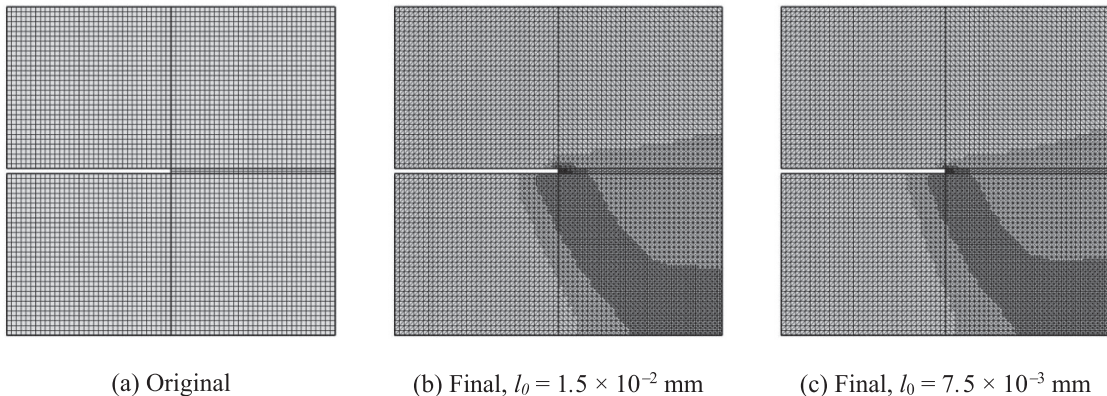


Fig. 8. Meshes of the 2D Single-edge-notched square subjected to shear loading.

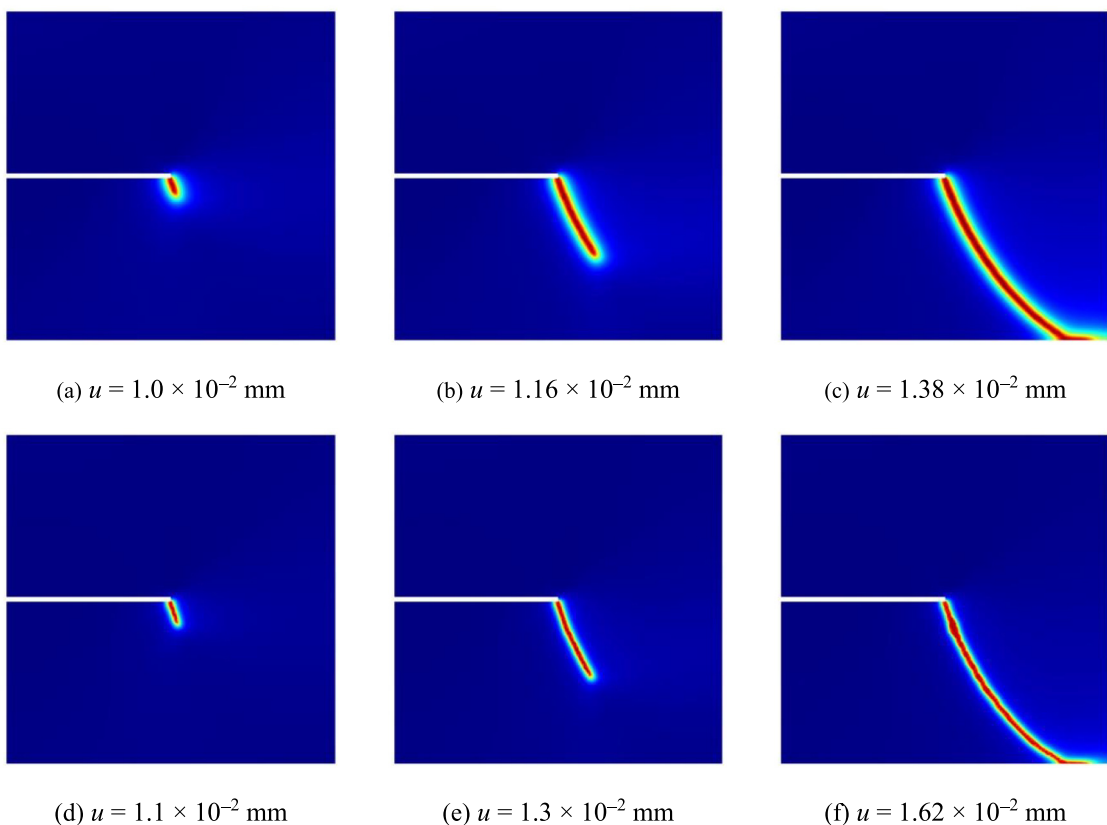


Fig. 9. Crack pattern of 2D Single-edge-notched square subjected to shear loading: (a), (b), (c) for a length scale  $l_0$  of  $1.5 \times 10^{-2}$  mm and (d), (e), and (f) for a length scale  $l_0$  of  $7.5 \times 10^{-3}$  mm.

(Cai, 2013; Zhou & Wang, 2016). A typical Brazilian disc tests exhibits typical geometry and boundary conditions as shown in Fig. 11.

The following material parameters are used:  $\rho = 2630 \text{ kg/m}^3$ ,  $E = 90 \text{ GPa}$ , and  $\nu = 0.3$ . We use three length scale parameters, namely  $l_0 = 1, 2$ , and  $3 \text{ mm}$ . With respect to the adaptive phase field method, an original mesh that consists of 6-node quadratic elements with a maximum

element size of 4 mm is used as shown in Fig. 12. Specifically,  $k = 1 \times 10^{-9}$  is selected to avoid numerical singularity during calculation. Finally, we conduct the simulation by using the following five different  $G_c$ : 5, 10, 15, 20, and 25 J/m<sup>2</sup>, respectively.

With respect to  $l_0 = 2$  mm, the final mesh obtained in the adaptive phase field method for different  $G_c$  is shown in Fig. 13. After continuous adaptive remeshing, meshes

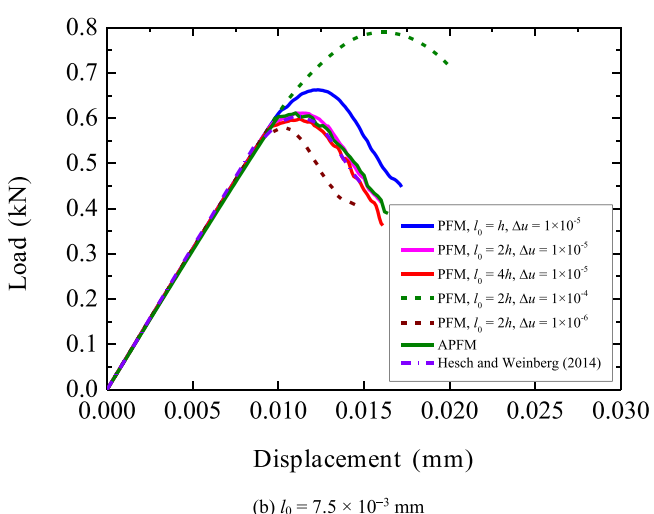
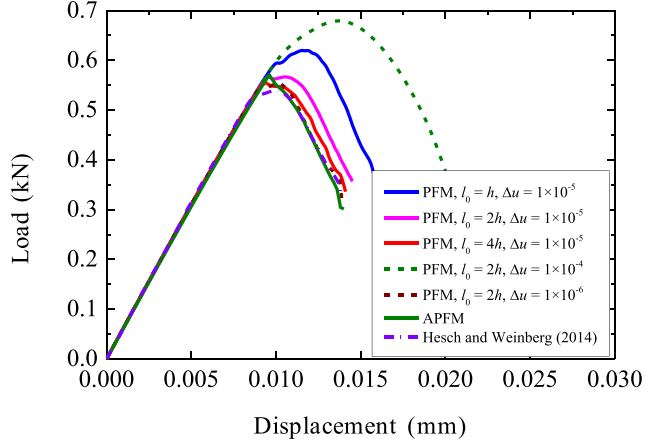


Fig. 10. Load-displacement curves of the 2D single-edge-notched square subjected to shear.

with a lower size concentrate in the center of the Brazilian specimen where fractures initiate and propagate. Fig. 14 presents the crack initiation and propagation in the Brazil splitting test for  $G_c = 15 \text{ J/m}^2$  and  $l_0 = 2 \text{ mm}$ . As shown in the figure, when the displacement  $u = 1.8 \times 10^{-2} \text{ mm}$ , the crack initiates in the center of the disc where the maximum tensile stress occurs. The aforementioned numerical observation is in good agreement with extant experimental and analytical results (Atkinson et al., 1982; Entacher et al., 2015). When  $u = 1.802 \times 10^{-2} \text{ mm}$ , the crack propagates and its width increases. A continuous crack propagation is subsequently observed when the crack tips move towards the upper and bottom ends of the specimen when  $u$  reaches  $1.804 \times 10^{-2} \text{ mm}$ . Given the locally compressed area around the ends of the specimen, it is not possible for the crack to deeply penetrate into the ends, and we observe crack branching when  $u$  reaches  $1.809 \times 10^{-2} \text{ mm}$ .

Figure 15 presents the curves of the reaction force on the upper end of the Brazilian disc versus the displacement  $u$  for different  $G_c$  values. As shown in the figure, a sudden

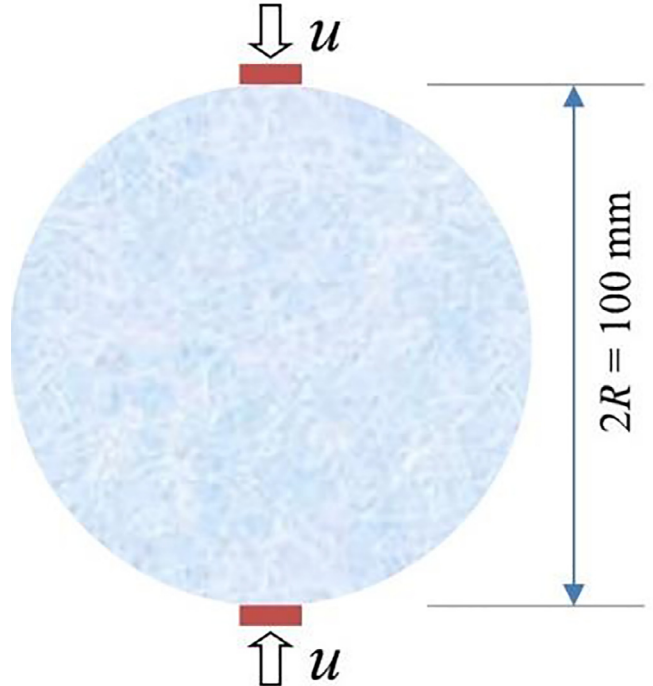


Fig. 11. Geometry and boundary condition of a Brazil splitting test.

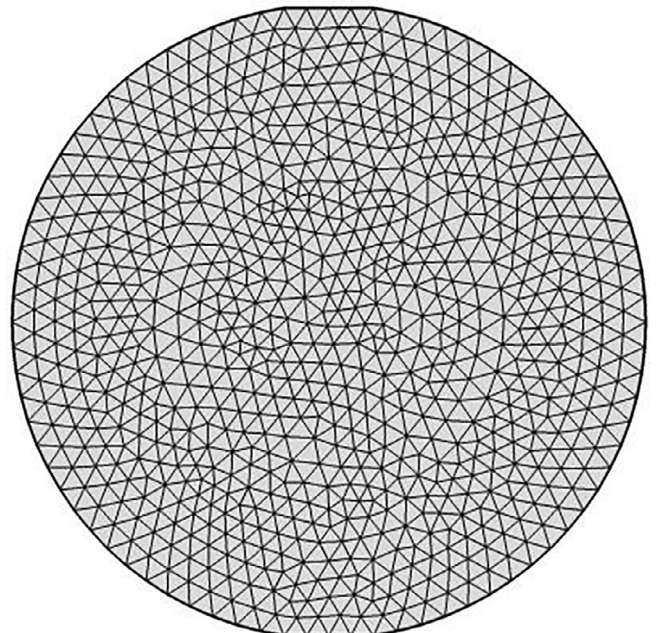
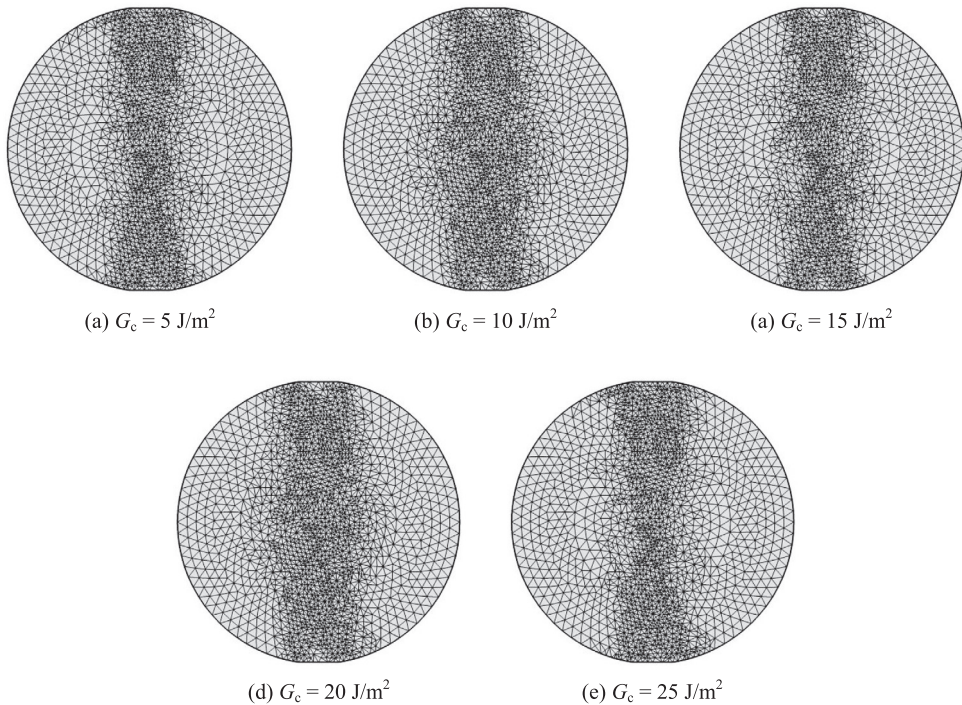
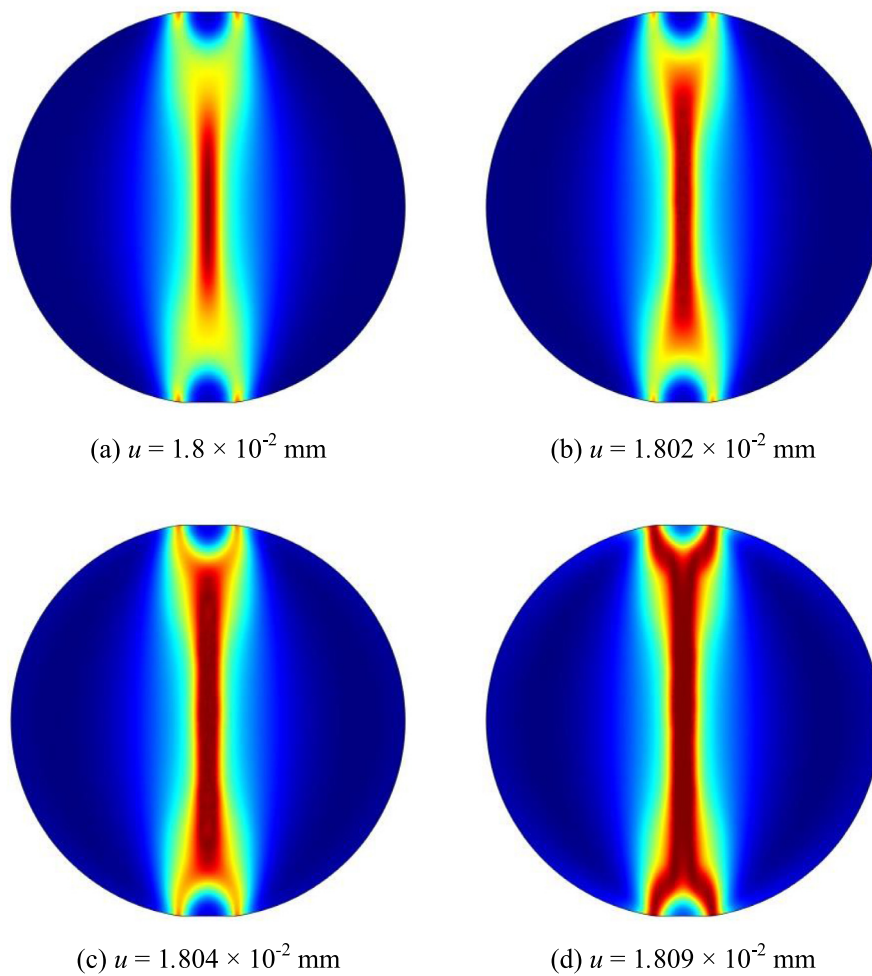


Fig. 12. Original mesh of the Brazil specimen.

drop in the load occurs after the phase field increases to 1. Furthermore, the peak load increases with increases in  $G_c$ . The tensile strength  $\sigma_t$  of the Brazilian specimen is given as follows:

$$\sigma_t = \frac{2P_{\text{peak}}}{\pi D L}, \quad (13)$$

Fig. 13. Final mesh under different  $G_c$ .Fig. 14. Crack propagation of the Brazil splitting test at a displacement for  $G_c = 15 \text{ J/m}^2$ .

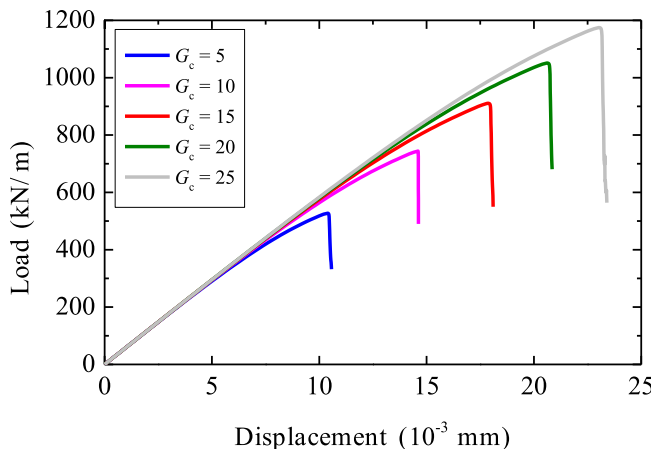


Fig. 15. Load-displacement curves for the Brazil splitting test under different  $G_c$ .

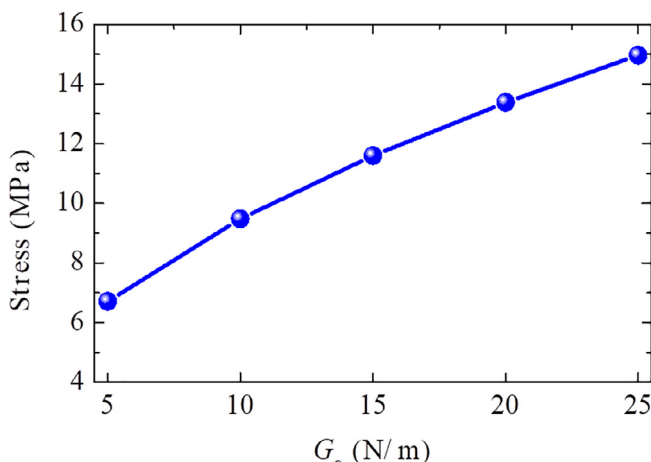


Fig. 16. Tensile strength by the Brazil splitting tests under different  $G_c$ .

where  $P_{\text{peak}}$  denotes the peak load, and  $D$  and  $L$  denote the diameter and length of the Brazilian specimen. Thus, we present the tensile strength by the phase field simulation in Fig. 16. The tensile strength increases at a decreasing rate with increases in  $G_c$ .

The final meshes used by the adaptive phase field method under different  $l_0$  values are shown in Fig. 17. A high mesh density is also observed in the center of the specimen. Fig. 18 shows the final crack pattern under different  $l_0$  values, and similar cracks are obtained with a slight difference in the width. An increase in the  $l_0$  increases the crack width. The load–displacement curves under different  $l_0$  values are shown in Fig. 19, and the tensile strength of the specimen under different  $l_0$  values are presented in Fig. 20. The tensile strength decreases with increases in  $l_0$ .

We subsequently test the influence of the specimen diameter  $D$ . Figs. 21 and 22 present the load–displacement curves and the tensile strength for Brazil splitting tests under different specimen diameters, respectively. As shown in the figure, the peak load of the specimen increases with increases in diameter  $D$ . However, the tensile strength is slightly affected by the diameter.

We also compare the load–displacement curve obtained by the APFM with the experimental results in Fig. 23. The experimental curve was first reported in a study by Erarslan and Williams (2012). It should be noted that there are a few adjustments in the parameters as follows:  $D = 52$  mm,  $E = 31.5$  GPa,  $\nu = 0.25$ , a length scale parameter of  $l_0 = 1$  mm, and a maximum element size of  $h = 0.5$  mm. Fig. 23 shows that the APFM reproduces the experimental results well. The main reason for the difference in Fig. 23 is the contact issue in the actual Brazilian test.

## 5.2 Notched semi-circular bend (NSCB) tests

We consider a rock specimen in a notched semi-circular bend (NSCB) test, and the crack initiation and propagation are simulated. Geometry and boundary condition of the rock specimen are shown in Fig. 24. The mechanical properties of Laurentian granite (LG) (Gao et al., 2015) are used. Therefore, the rock density  $\rho$  is 2 630 kg/m<sup>3</sup>, Young's modulus  $E$  is 92 GPa, and Poisson's ratio  $\nu$  is 0.21. We select  $G_c = 5.6, 6.6, 7.6, 8.6$ , and  $9.6$  J/m<sup>2</sup>. We also test the influence of  $l_0$ , and set  $l_0 = 3 \times 10^{-4}$  m,  $4.5 \times 10^{-4}$  m, and  $6 \times 10^{-4}$  m. A vertical displacement on the top of the

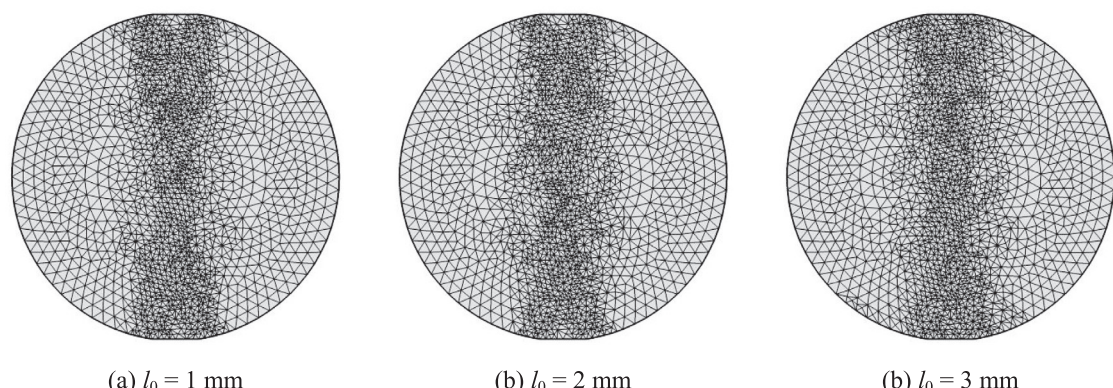


Fig. 17. Final mesh of the Brazilian specimen under different  $l_0$ .

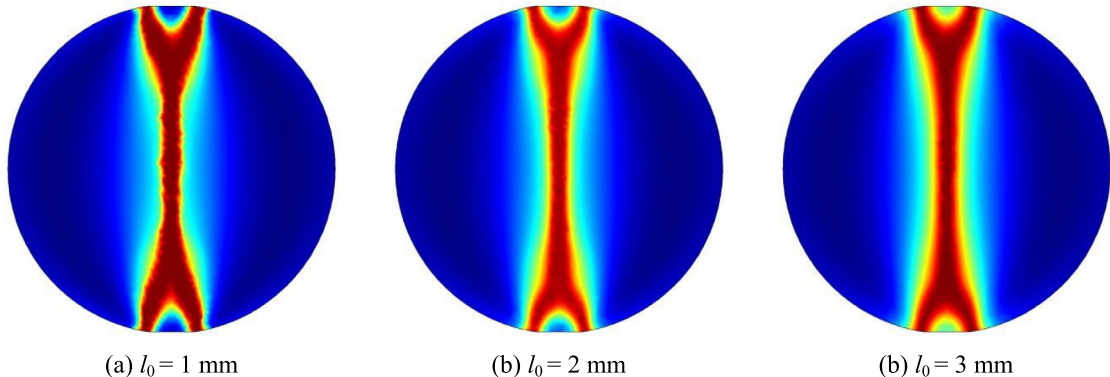


Fig. 18. Final crack pattern of the Brazilian specimen under different  $l_0$ .

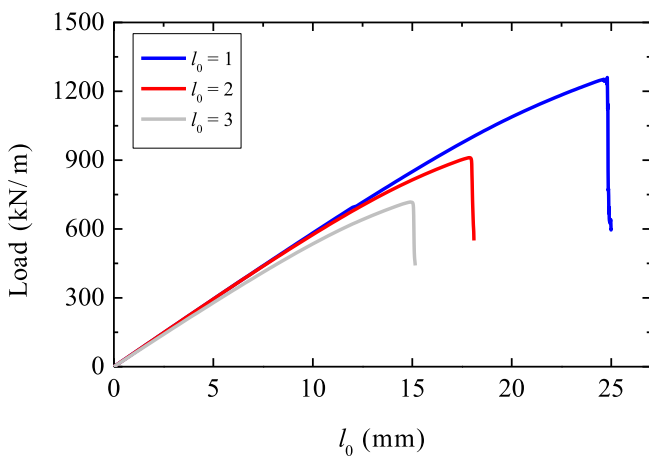


Fig. 19. Load-displacement curves for the Brazil splitting test under different  $l_0$ .

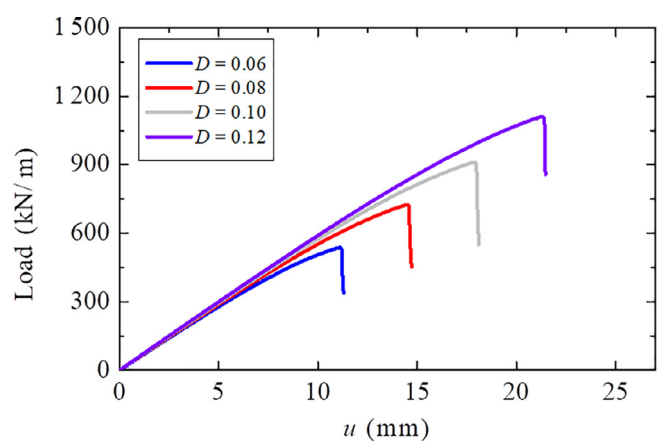


Fig. 21. Load-displacement curves for the Brazil splitting test under different specimen diameter.

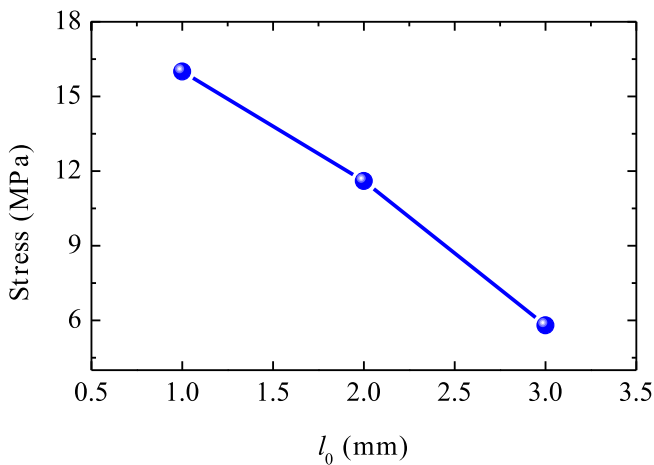


Fig. 20. Tensile strength by Brazil splitting tests under different  $l_0$ .

specimen is applied to drive crack propagation from the tip of the notch, and we apply a displacement increment  $\Delta u = 5 \times 10^{-7}$  mm in each time step.

In the original mesh (**Fig. 25a**), 6-node quadratic triangular elements are used, and the maximum element

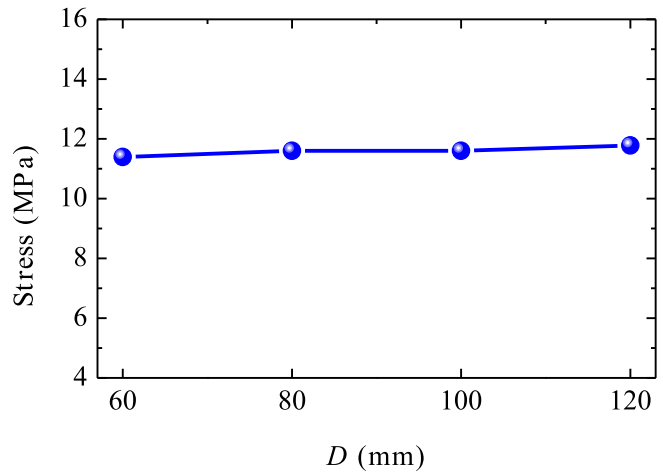


Fig. 22. Tensile strength by Brazil splitting tests under different specimen diameter.

size is 0.0018 m. However, as shown in Fig. 25b, the adaptive phase field method refines the mesh around the crack path in the final time step for  $G_c = 7.6 \text{ J/m}^2$  and  $l_0 = 4.5 \times 10^{-4} \text{ m}$ .

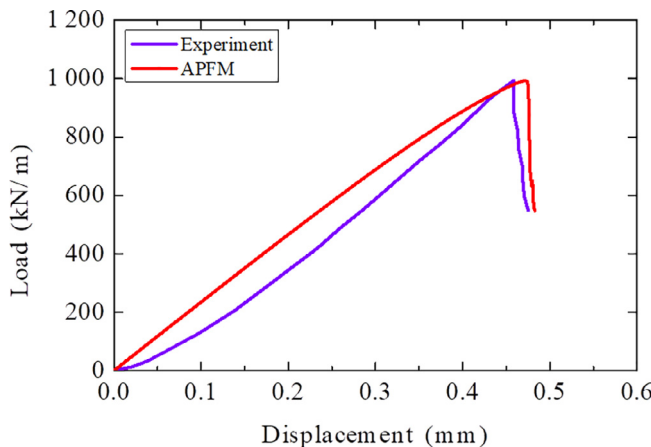


Fig. 23. Comparison of the load-displacement curves obtained by the experimental test and APFM.

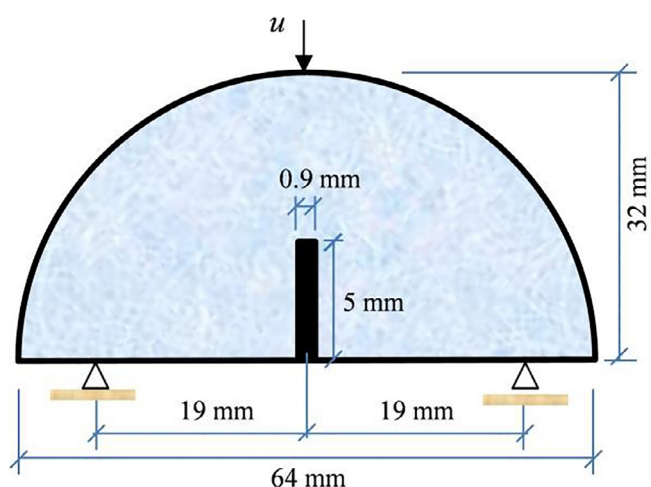


Fig. 24. Geometry and boundary condition of the notched semi-circular bend (NSCB) tests.

Figure 26 shows the crack initiation and propagation in the NSCB specimen by using the adaptive phase field model for  $G_c = 7.6 \text{ J/m}^2$  and  $l_0 = 4.5 \times 10^{-4} \text{ m}$ . As shown in the figure, the crack is initiated from the tip of the notch when the applied displacement  $u$  reaches  $6.72 \times 10^{-3} \text{ mm}$ .

When  $u$  reaches  $6.74 \times 10^{-3} \text{ mm}$  and  $6.77 \times 10^{-3} \text{ mm}$ , a straight crack is observed in the vertical direction. When the displacement  $u$  reaches  $6.86 \times 10^{-3} \text{ mm}$ , the crack propagates close to the upper end of the NSCB specimen, and specimen failure is observed. It should be noted that the crack patterns obtained by the adaptive phase field method are consistent with the experimental results indicated by Gao et al. (2015).

Additionally, the adaptive phase field simulations show that  $G_c$  does not significantly affect the crack patterns, and different  $G_c$  exhibit the same crack patterns. Under different  $G_c$ , the curves of the reaction force on the upper end of the specimen versus the applied displacement are shown in Fig. 27. A sudden drop in the load is observed after the crack initiation due to brittle fracture. The same slope is also observed for all curves before failure while the peak load increases when  $G_c$  increases.

In order to test the influence of the length scale  $l_0$ , we present the final crack patterns under different  $l_0$  values in Fig. 28. The load-displacement curves of the NSCB specimen under different  $l_0$  values are presented in Fig. 29. As shown in the figure, increases in the  $l_0$  values increase the peak load.

### 5.3 3D NSCB tests

We consider a 3D NSCB test in the last example. Propagation of a quasi-static crack in a 3D NSCB specimen is simulated. The geometry and boundary conditions of the specimen are similar to the 2D tests, and the thickness of the 3D specimen is 16 mm. Parameters identical to those in 2D tests are used when  $G_c = 7.6 \text{ J/m}^2$ . During the calculation, the displacement increment  $\Delta u = 2.5 \times 10^{-7} \text{ mm}$  is applied.

The meshes used in the 3D simulation is shown in Fig. 30. In the original mesh, the maximum element size is 1.8 mm, and the mesh density increases after the use of adaptive remeshing technology. Fig. 31 presents the crack propagation at the displacements  $u = 7.203 \times 10^{-3} \text{ mm}$ ,  $7.230 \times 10^{-3} \text{ mm}$ , and  $7.270 \times 10^{-3} \text{ mm}$ . The crack patterns are identical to those in the 2D simulation. The simulated crack pattern is also consistent with the

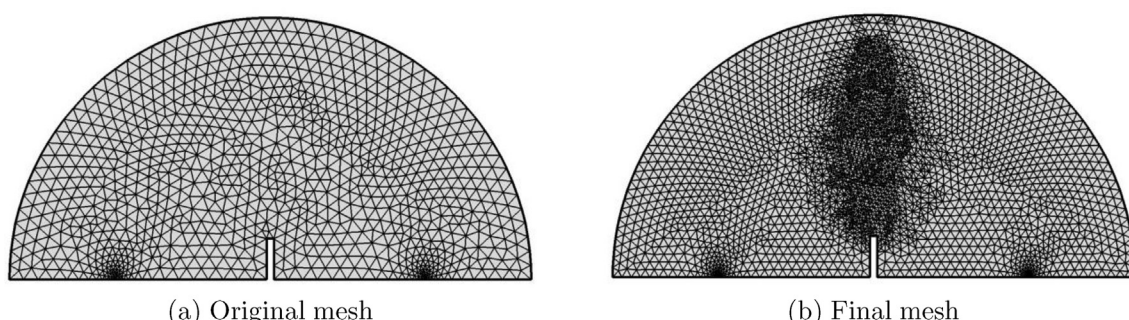
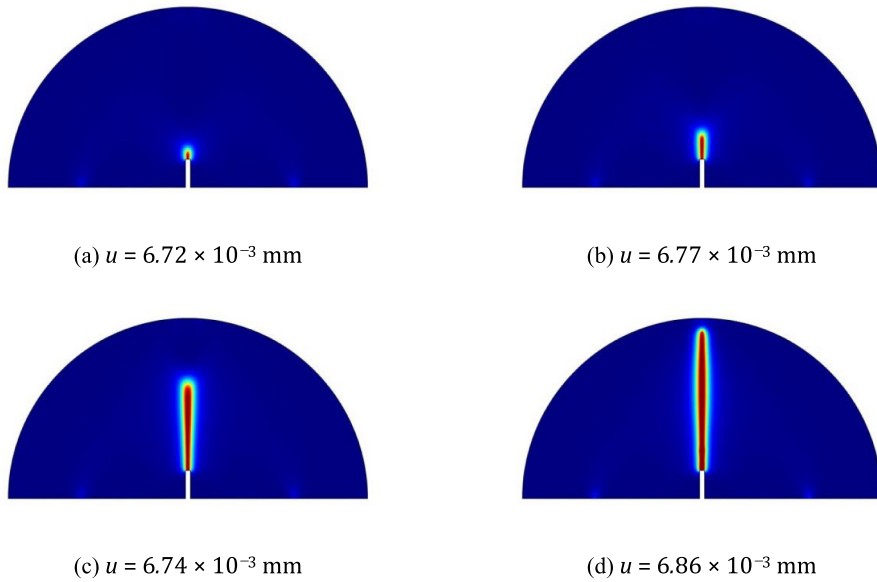
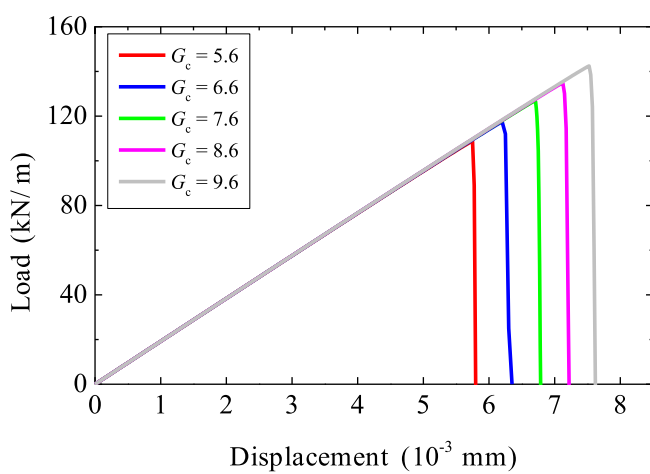
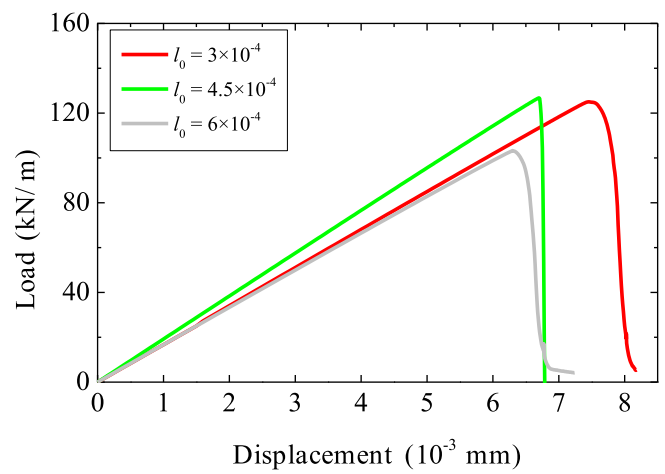


Fig. 25. Meshes of the NSCB tests.

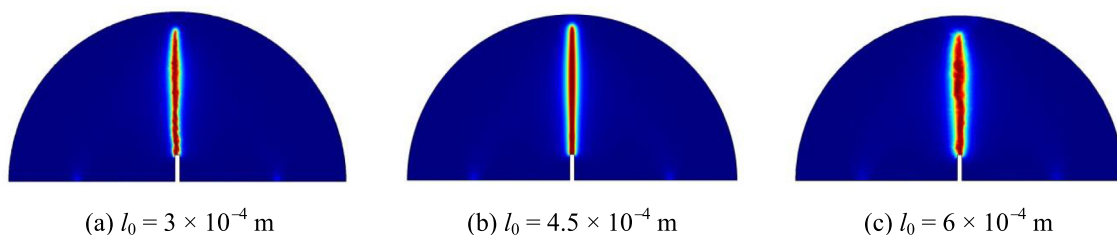
Fig. 26. Crack propagation of the NSCB tests at a displacement for  $G_c = 7.6 \text{ J/m}^2$ .Fig. 27. Load-displacement curves of the NSCB tests under different  $G_c$ .

experimental observations (Gao et al., 2015). The load–displacement curve on the upper end of the specimen is shown in Fig. 32. The trend of the curve is similar to that in 2D figures, and a sudden drop in the applied load is observed due to brittle fracture. The success in the simulation of the 3D NSCB test verifies the ability and practicability of the

Fig. 29. Load-displacement curves of the NSCB tests under different  $l_0$ .

APFM in modeling quasi-static crack propagation of rocks in 3D.

Although the APFM exhibits promising advantages for modeling fractures, it still includes an intrinsic defect for the application in rocks, and this should be improved in future studies. Shear cracks cannot be predicted by APFM

Fig. 28. Final crack patterns of the NSCB tests under different  $l_0$ .

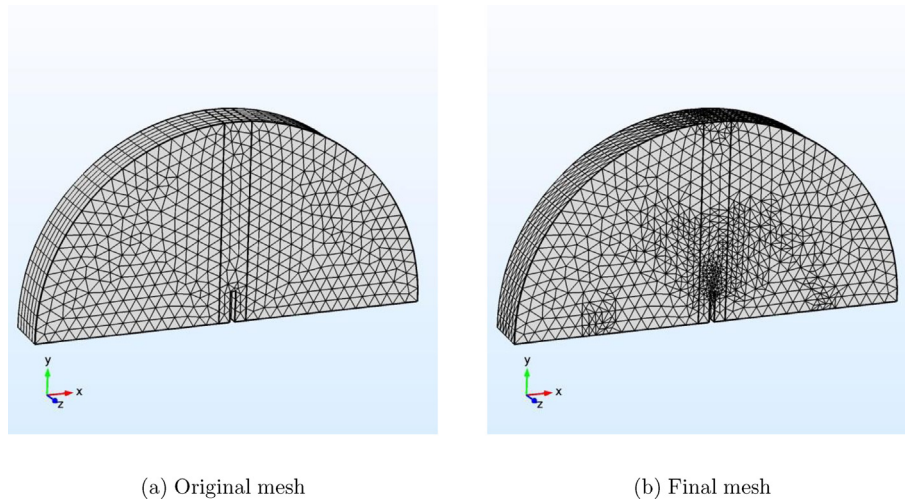


Fig. 30. Meshes of the 3D NSCB tests.

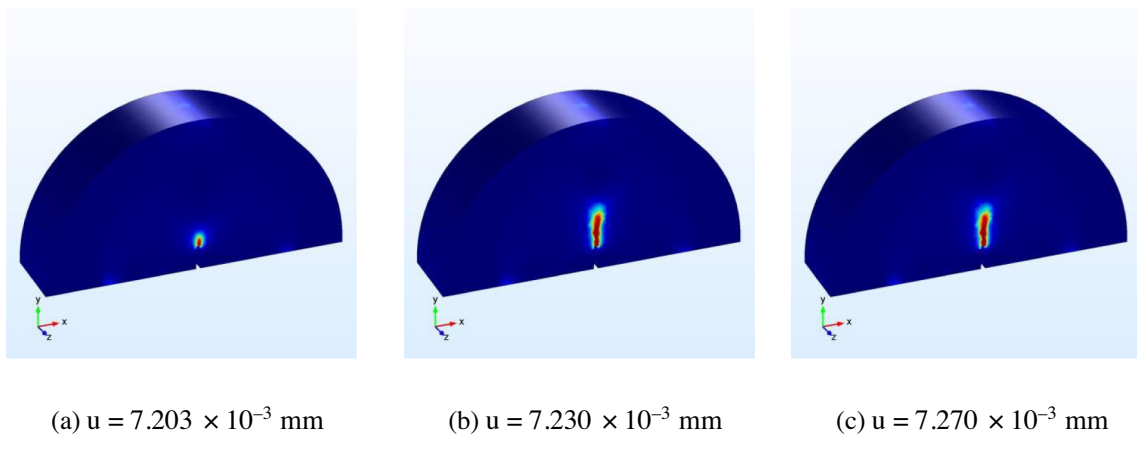
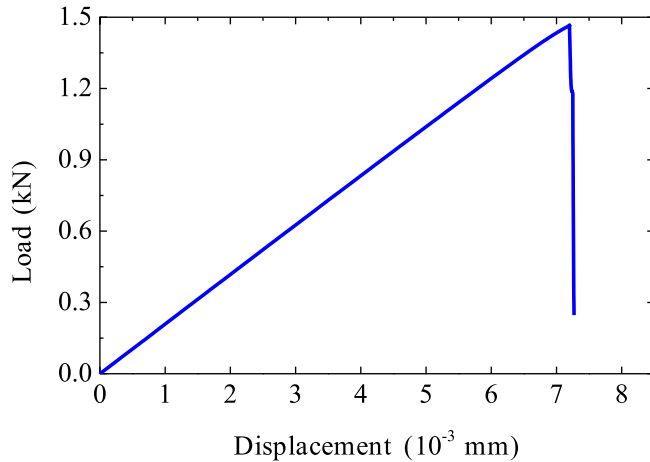
Fig. 31. Crack propagation of the 3D NSCB test at a displacement for  $G_c = 7.6 \text{ J/m}^2$ .

Fig. 32. Load-displacement curve of the 3D NSCB test.

when a rock reaches its shear strength because the shear strength is not involved in the formulation of the phase field method. The formulation used in the study only involves elastic energy that drives crack propagation.

## 6 Conclusion

We present an adaptive phase field method for modeling quasi-static crack propagation in rocks. Crack initiation due to positive strains is considered, and a numerical scheme is implemented by using commercial software, COMSOL Multiphysics. Two benchmark tests are first examined, namely, a single-edge-notched square plate subject to respective tension and shear loadings. Subsequently, the crack propagation in Brazil splitting tests, 2D notched semi-circular bend (NSCB) tests, and 3D NSCB tests is simulated and analyzed. The simulated results are in good agreement with the experimental observations, thereby indicating the feasibility and practicability of the adaptive phase field method in rocks (even in 3D cases).

All the numerical examples presented in the study indicate that the propagation of the cracks is autonomous and no external fracture criteria are required for phase field modeling. Furthermore, the adaptive remeshing scheme reduces unnecessary globally mesh refinement and exhibits good adaptability for fracture modeling. Therefore, the

adaptive phase field modeling will be extended to other crack problems in rock engineering in a future study.

## Acknowledgement

The authors gratefully acknowledge financial support provided by the Sino-German (CSC-DAAD) Postdoc Scholarship Program 2016.

## References

- Amiri, F., Anitescu, C., Arroyo, M., Bordas, S. P. A., & Rabczuk, T. (2014). XLME interpolants, a seamless bridge between xfem and enriched meshless methods. *Computational Mechanics*, 53(1), 45–57.
- Anderson, T. L. (2005). *Fracture mechanics: Fundamentals and applications*. CRC Press.
- Areias, P., Msekh, M., & Rabczuk, T. (2016a). Damage and fracture algorithm using the screened poisson equation and local remeshing. *Engineering Fracture Mechanics*, 158, 116–143.
- Areias, P., & Rabczuk, T. (2013). Finite strain fracture of plates and shells with configurational forces and edge rotations. *International Journal for Numerical Methods in Engineering*, 94(12), 1099–1122.
- Areias, P., & Rabczuk, T. (2017). Steiner-point free edge cutting of tetrahedral meshes with applications in fracture. *Finite Elements in Analysis and Design*, 132, 27–41.
- Areias, P., Rabczuk, T., & Camanho, P. (2014). Finite strain fracture of 2d problems with injected anisotropic softening elements. *Theoretical and Applied Fracture Mechanics*, 72(1), 50–63.
- Areias, P., Rabczuk, T., & Dias-da Costa, D. (2013). Element-wise fracture algorithm based on rotation of edges. *Engineering Fracture Mechanics*, 110, 113–137.
- Areias, P., Rabczuk, T., & Msekh, M. (2016b). Phase-field analysis of finite-strain plates and shells including element subdivision. *Computer Methods in Applied Mechanics and Engineering*, 312, 322–350.
- Atkinson, C., Smelser, R., & Sanchez, J. (1982). Combined mode fracture via the cracked brazilian disk test. *International Journal of Fracture*, 18(4), 279–291.
- Badawy, M. F., Msekh, M. A., Hamdia, K. M., Steiner, M. K., Lahmer, T., & Rabczuk, T. (2017). Hybrid nonlinear surrogate models for fracture behavior of polymeric nanocomposites. *Probabilistic Engineering Mechanics*, 50, 64–75.
- Badnava, H., Msekh, M. A., Etemadi, E., & Rabczuk, T. (2018). An h-adaptive thermo-mechanical phase field model for fracture. *Finite Elements in Analysis and Design*, 138, 31–47.
- Belytschko, T., & Lin, J. I. (1987). A three-dimensional impact-penetration algorithm with erosion. *International Journal of Impact Engineering*, 5(1–4), 111–127.
- Bobet, A., & Einstein, H. (1998). Fracture coalescence in rock-type materials under uniaxial and biaxial compression. *International Journal of Rock Mechanics and Mining Sciences*, 35(7), 863–888.
- Borden, M. J., Verhoosel, C. V., Scott, M. A., Hughes, T. J., & Landis, C. M. (2012). A phase-field description of dynamic brittle fracture. *Computer Methods in Applied Mechanics and Engineering*, 217, 77–95.
- Bourdin, B., Francfort, G. A., & Marigo, J.-J. (2008). The variational approach to fracture. *Journal of Elasticity*, 91(1), 5–148.
- Cai, M. (2013). Fracture initiation and propagation in a Brazilian disc with a plane interface: A numerical study. *Rock Mechanics and Rock Engineering*, 46(2), 289–302.
- Chau-Dinh, T., Zi, G., Lee, P. S., Rabczuk, T., & Song, J. H. (2012). Phantom-node method for shell models with arbitrary cracks. *Computers & Structures*, 92, 242–256.
- Comsol, A., 2005. Comsol multiphysics user\_s guide. Version: September 10, 333.
- Entacher, M., Schuller, E., & Galler, R. (2015). Rock failure and crack propagation beneath disc cutters. *Rock Mechanics and Rock Engineering*, 48(4), 1559–1572.
- Earslan, N., & Williams, D. (2012). Investigating the effect of cyclic loading on the indirect tensile strength of rocks. *Rock Mechanics and Rock Engineering*, 45(3), 327–340.
- Gao, G., Huang, S., Xia, K., & Li, Z. (2015). Application of digital image correlation (DIC) in dynamic notched semi-circular bend (NSCB) tests. *Experimental Mechanics*, 55(1), 95–104.
- Hamdia, K. M., Msekh, M. A., Silani, M., Vu-Bac, N., Zhuang, X., Nguyen-Thoi, T., & Rabczuk, T. (2015). Uncertainty quantification of the fracture properties of polymeric nanocomposites based on phase field modeling. *Composite Structures*, 133, 1177–1190.
- Hamdia, K. M., Silani, M., Zhuang, X., He, P., & Rabczuk, T. (2017). Stochastic analysis of the fracture toughness of polymeric nanoparticle composites using polynomial chaos expansions. *International Journal of Fracture*, 206(2), 215–227.
- Hesch, C., & Weinberg, K. (2014). Thermodynamically consistent algorithms for a finite deformation phase-field approach to fracture. *International Journal for Numerical Methods in Engineering*, 99(12), 906–924.
- Johnson, G. R., & Stryk, R. A. (1987). Eroding interface and improved tetrahedral element algorithms for high-velocity impact computations in three dimensions. *International Journal of Impact Engineering*, 5(1–4), 411–421.
- Lee, H., & Jeon, S. (2011). An experimental and numerical study of fracture coalescence in pre-cracked specimens under uniaxial compression. *International Journal of Solids and Structures*, 48(6), 979–999.
- Miehe, C., Hofacker, M., & Welschinger, F. (2010a). A phase field model for rate-independent crack propagation: Robust algorithmic implementation based on operator splits. *Computer Methods in Applied Mechanics and Engineering*, 199(45), 2765–2778.
- Miehe, C., Welschinger, F., & Hofacker, M. (2010b). Thermodynamically consistent phase-field models of fracture: Variational principles and multi-field FE implementations. *International Journal for Numerical Methods in Engineering*, 83(10), 1273–1311.
- Möes, N., & Belytschko, T. (2002). Extended finite element method for cohesive crack growth. *Engineering Fracture Mechanics*, 69(7), 813–833.
- Msekh, M. A., Cuong, N. H., Zi, G., Areias, P., Zhuang, X., & Rabczuk, T. (2017). Fracture properties prediction of clay/epoxy nanocomposites with interphase zones using a phase field model. *Engineering Fracture Mechanics*.
- Nanthakumar, S., Lahmer, T., & Rabczuk, T. (2014). Detection of multiple flaws in piezoelectric structures using XFEM and level sets. *Computer Methods in Applied Mechanics and Engineering*, 275, 98–112.
- Park, C., & Bobet, A. (2009). Crack coalescence in specimens with open and closed flaws: A comparison. *International Journal of Rock Mechanics and Mining Sciences*, 46(5), 819–829.
- Park, C., & Bobet, A. (2010). Crack initiation, propagation and coalescence from frictional flaws in uniaxial compression. *Engineering Fracture Mechanics*, 77(14), 2727–2748.
- Pijaudier-Cabot, G., Haidar, K., & Dub'e, J.-F. (2004). Non-local damage model with evolving internal length. *International Journal for Numerical and Analytical Methods in Geomechanics*, 28(7–8), 633–652.
- Rabczuk, T., Areias, P., & Belytschko, T. (2007a). A simplified mesh-free method for shear bands with cohesive surfaces. *International Journal for Numerical Methods in Engineering*, 69(5), 993–1021.
- Rabczuk, T., & Belytschko, T. (2004). Cracking particles: A simplified meshfree method for arbitrary evolving cracks. *International Journal for Numerical Methods in Engineering*, 61(13), 2316–2343.
- Rabczuk, T., & Belytschko, T. (2007). A three-dimensional large deformation meshfree method for arbitrary evolving cracks. *Computer Methods in Applied Mechanics and Engineering*, 196(29–30), 2777–2799.
- Rabczuk, T., Bordas, S., & Zi, G. (2007b). A three-dimensional meshfree method for continuous multiple-crack initiation, propagation and junction in statics and dynamics. *Computational Mechanics*, 40(3), 473–495.
- Rabczuk, T., & Ren, H. (2017). A peridynamics formulation for quasi-static fracture and contact in rock. *Engineering Geology*, 225, 42–48.
- Rabczuk, T., & Samaniego, E. (2008). Discontinuous modelling of shear bands using adaptive meshfree methods. *Computer Methods in Applied Mechanics and Engineering*, 197(6), 641–658.
- Rabczuk, T., & Zi, G. (2007). A meshfree method based on the local partition of unity for cohesive cracks. *Computational Mechanics*, 39(6), 743–760.
- Rabczuk, T., Zi, G., Bordas, S., & Nguyen-Xuan, H. (2008a). A geometrically nonlinear three-dimensional cohesive crack method for reinforced concrete structures. *Engineering Fracture Mechanics*, 75(16), 4740–4758.
- Rabczuk, T., Zi, G., Bordas, S., & Nguyen-Xuan, H. (2010). A simple and robust three-dimensional cracking-particle method without enrichment. *Computer Methods in Applied Mechanics and Engineering*, 199(37), 2437–2455.

- Rabczuk, T., Zi, G., Gerstenberger, A., & Wall, W. A. (2008b). A new crack tip element for the phantom-node method with arbitrary cohesive cracks. *International Journal for Numerical Methods in Engineering*, 75(5), 577–599.
- Ren, H., Zhuang, X., Cai, Y., & Rabczuk, T. (2016). Dual-horizon peridynamics. *International Journal for Numerical Methods in Engineering*, 108(12), 1451–1476.
- Ren, H., Zhuang, X., & Rabczuk, T. (2017). Dual-horizon peridynamics: A stable solution to varying horizons. *Computer Methods in Applied Mechanics and Engineering*, 318, 762–782.
- Sagong, M., & Bobet, A. (2002). Coalescence of multiple flaws in a rock-model material in uniaxial compression. *International Journal of Rock Mechanics and Mining Sciences*, 39(2), 229–241.
- Song, J. H., Wang, H., & Belytschko, T. (2008). A comparative study on finite element methods for dynamic fracture. *Computational Mechanics*, 42(2), 239–250.
- Thai, T. Q., Rabczuk, T., Bazilevs, Y., & Meschke, G. (2016). A higher-order stress-based gradient-enhanced damage model based on isogeometric analysis. *Computer Methods in Applied Mechanics and Engineering*, 304, 584–604.
- Vu-Bac, N., Lahmer, T., Zhuang, X., Nguyen-Thoi, T., & Rabczuk, T. (2016). A software framework for probabilistic sensitivity analysis for computationally expensive models. *Advances in Engineering Software*, 100, 19–31.
- Vu-Bac, N., Nguyen-Xuan, H., Chen, L., Lee, C. K., Zi, G., Zhuang, X., ... Rabczuk, T. (2013). A phantom-node method with edge-based strain smoothing for linear elastic fracture mechanics. *Journal of Applied Mathematics*, 2013. <https://doi.org/10.1155/2013/978026>.
- Wong, L., & Einstein, H. (2009). Crack coalescence in molded gypsum and Carrara marble: Part 1. Macroscopic observations and interpretation. *Rock Mechanics and Rock Engineering*, 42(3), 475–511.
- Wong, R. H. C., Chau, K. T., Tang, C. A., & Lin, P. (2001). Analysis of crack coalescence in rock-like materials containing three flaws – Part i: Experimental approach. *International Journal of Rock Mechanics and Mining Sciences*, 38(7), 909–924.
- Zhou, X., Cheng, H., & Feng, Y. (2014). An experimental study of crack coalescence behaviour in rock-like materials containing multiple flaws under uniaxial compression. *Rock Mechanics and Rock Engineering*, 47 (6), 1961–1986.
- Zhou, X. P., & Wang, Y. T. (2016). Numerical simulation of crack propagation and coalescence in pre-cracked rock-like Brazilian disks using the non-ordinary state-based peridynamics. *International Journal of Rock Mechanics and Mining Sciences*, 89, 235–249.